Mitigation of the internal *p-n* junction in math xmlns="http://www.w3.org/1998/Math/MathML">mrow>msub>mi>CoS/mi>mn>2/mn>/msub>/mrow>/math>-contacted math xmlns="http://www.w3.org/1998/Math/MathML">mrow>msub>mi>FeS/mi>mn>2/mn>/msub>/mrow>/math> single crystals: Accessing bulk semiconducting transport

Bryan Voigt, Bhaskar Das, David M. Carr, Debmalya Ray, Moumita Maiti, William Moore, Michael Manno, Jeff Walter, Eray S. Aydil, and Chris Leighton

Phys. Rev. Materials **5**, 025405 — Published 26 February 2021

DOI: 10.1103/PhysRevMaterials.5.025405

Resubmitted to *Phys. Rev. Materials* on 2/10/2020

Mitigation of the internal *p-n* junction in CoS_2-contacted FeS_2 single crystals: Accessing bulk semiconducting transport

Bryan Voigt[1], Bhaskar Das[1], David M. Carr[2], Debmalya Ray[3], Moumita Maiti[1], William Moore[1], Michael Manno[1], Jeff Walter[1,4], Eray S. Aydil*[5] and Chris Leighton*[1]

[1]*Department of Chemical Engineering and Materials Science,*
University of Minnesota, Minneapolis, MN 55455, USA

[2]*Physical Electronics, Inc.,*
Chanhassen, MN 55317, USA

[3]*Department of Chemistry,*
University of Minnesota, Minneapolis, MN 55455, USA

[4]*Department of Physics,*
Augsburg University, Minneapolis, MN 55454, USA

[5]*Department of Chemical and Biomolecular Engineering,*
New York University Tandon School of Engineering, Brooklyn, NY 11201, USA

ABSTRACT: Pyrite FeS_2 is an outstanding candidate for a low cost, nontoxic, sustainable photovoltaic material, but efficient pyrite-based solar cells are yet to materialize. Recent studies of single crystals have shed much light on this by uncovering a *p*-type surface inversion layer on *n*-type (S-vacancy-doped) crystals, and the resulting internal *p-n* junction. This leaky internal junction likely plays a key role in limiting efficiency in pyrite-based photovoltaic devices, also obscuring the true bulk semiconducting transport properties of pyrite crystals. Here, we demonstrate complete mitigation of the internal *p-n* junction in FeS_2 crystals by fabricating metallic CoS_2 contacts *via* a process that simultaneously diffuses Co (a shallow donor) into the crystal, the resulting heavy *n*-doping yielding direct ohmic contact to the interior. Low-temperature bulk transport studies of controllably Co- and S-vacancy-doped semiconducting crystals then enable a host of previously inaccessible observations and measurements, including: Determination of donor activation energies (which are as low as 5 meV for Co), observation of an unexpected second activated transport regime, realization of electron mobility up to 2100 $cm^2V^{-1}s^{-1}$, elucidation of very different mobilities in Co- and V_S-doped cases, and observation of an abrupt temperature-dependent crossover to bulk Efros-Shklovskii variable-range hopping, accompanied by an unusual form of non-linear Hall effect. Aspects of the results are interpreted with the aid of first-principles electronic structure calculations on both Co- and S-vacancy-doped FeS_2. This work thus demonstrates unequivocal mitigation of the internal *p-n* junction in pyrite single crystals, with important implications for both future fundamental studies and photovoltaic devices.

*Corresponding authors: leighton@umn.edu, aydil@nyu.edu

I. INTRODUCTION

Due to outstanding visible light absorption, adequate electron mobility and minority carrier diffusion length, exceptionally low cost [1], and earth-abundant nontoxic constituents [1], pyrite-structure FeS_2 has long been considered an attractive sustainable photovoltaic material [2]. Pyrite-based heterojunction solar cells have disappointing power conversion efficiencies, however (typically <3 %), limited by low open-circuit voltages (V_{OC}), even in single-crystal devices [2–7]. While historically a matter of debate [2–7], recent work provides compelling evidence that the low V_{OC} originates in a leaky *p*-*n* junction *internal* to pyrite [7–10]. Specifically, several recent publications on high-quality single crystals report a nm-thick *p*-type inversion layer on the surface of unintentionally-*n*-doped pyrite [8,9,11], leading to the situation shown schematically in Fig. 1(a). Consistent with earlier observations of surface-state-driven pinning of the Fermi level near the valence band maximum [2,12–14], substantial near-surface band bending is thought to occur (Fig. 1(a)). In horizontal single-crystal transport measurements, conspicuous surface conduction then arises, the electrical resistivity (ρ) abruptly flattening on cooling as bulk carrier freeze-out leads to current shunting by the heavily-*p*-doped surface [9,11]. Such behavior has been quantitatively captured by two-channel (bulk and surface) modeling [9,11]. Strong evidence has also been accumulated that S-vacancy (V_S)-based native defects are present [2,14,15] and responsible for the unintentional bulk *n*-doping in such crystals (as in Fig. 1(a)) [16,17]. Experiments have identified a ~225 meV deep donor and linked it to V_S [16], while computational work implicates V_S *clusters* as the likely donors [17].

Most recently, ρ(*T*) measurements on single crystals with systematically controlled S vacancy concentration ($[V_S]$) directly revealed the internal junction between the *n*-type interior and *p*-type surface [10] (*i.e.*, the depletion region in Fig. 1(a)). At sufficiently high $[V_S]$ (*i.e.*, low bulk resistance), the exponential *T*-dependence of the internal *p*-*n* junction resistance was shown to abruptly cut off current to the crystal interior on cooling, leading to an abrupt 10^4-fold increase in ρ at ~130-200 K [10]. Three-channel [bulk, surface, junction (depletion region)] modeling describing the internal *p*-*n* interface as a Schottky junction was shown to quantitatively reproduce the [V_S]-dependent ρ(*T*), enabling extraction of junction barrier heights [10]. The latter exhibit significant variance even in nominally identical crystals, averaging to ~320 meV [10]. Given this low average barrier height (notably close to V_{OC} in pyrite-crystal-based heterojunction solar cells [2–7]), the distribution in barrier heights (consistent with the variability in such cells [2–7]), and the substantial voltage deficit relative to simple band bending expectations (≥750 meV, see Fig. 1(a)) [10], a leaky internal *p*-*n* junction was concluded to play a key role in limiting V_{OC}, and thus efficiency, in pyrite-based heterojunction photovoltaic devices [10]. In essence, devices such as prior metal/FeS_2 Schottky cells [6] were in reality likely metal/heavily *p*-doped FeS_2 surface/internal junction/bulk *n*-type FeS_2 heterostructures, the V_{OC} deriving largely from the internal *p*-*n* junction.

An important consequence of the above is that the bulk electronic transport properties of semiconducting pyrite FeS_2 single crystals have been inaccessible below ~200 K, due to obfuscation by the internal junction. With no cryogenic measurements of the *T*-dependent bulk ρ, Hall electron density, and Hall mobility, for example, essential characterization of the electronic transport mechanisms in pyrite remains lacking. Just some of the gaps in fundamental understanding include: the interplay between bulk diffusive and hopping transport and the general level of disorder in state-of-the-art FeS_2 crystals; accurate positions of the donor levels for known *n*-type pyrite dopants; the behavior of mobility *vs*. *T* and doping level for different donors, and thus the overall electronic quality in comparison to semiconductors such as Si; the relative importance of scattering from phonons, ionized impurities, and other defects; the nature of the approach to the insulator-metal transition (IMT) (which is of particular interest for deep donors such as V_S [16]); and the possibility of quantum transport (*e.g.*, Shubnikov-de Haas oscillations) in crystals doped beyond the IMT, which could elucidate additional important transport parameters. Such information is important not only fundamentally but also for applications, such as in photovoltaics. Sufficiently advanced understanding of doping, for example, could enable mitigation of V_S deep donor concentrations to improve V_{OC} [7,9], identification of ideal *n*-dopants for future pyrite PV devices, identification and characterization of workable *p*-dopants, and thus the development of future *homojunction* FeS_2 solar cells, which could side-step issues with surface states. A means to mitigate the internal *p-n* junction in pyrite single crystals, thereby enabling bulk transport characterization, is thus highly desirable.

We address this challenge here by demonstrating that appropriately fabricated CoS_2 thin film overlayers on FeS_2 bulk single crystals enable direct ohmic contact to the crystal interior. CoS_2 has the same pyrite structure as FeS_2 but $t_{2g}^6e_g^1$ electronic configuration (*cf.* $t_{2g}^6e_g^0$ in FeS_2), resulting in metallicity and ferromagnetism with a Curie temperature $T_C \approx 120$ K [18,19]. We form CoS_2 by *ex situ* sulfidation of Co films at elevated temperature in a S atmosphere [20], simultaneously inducing reaction of the Co film to CoS_2 and significant interdiffusion of Co into the FeS_2 crystal, as verified by time-of-flight secondary ion mass spectrometry (TOF-SIMS) depth profiling. As CoS_2 is metallic [19,20] and Co is a shallow donor in FeS_2 [10,21–24], this results in a metallic contact on an FeS_2 surface where heavy doping under the CoS_2 yields direct ohmic contact to the crystal interior (through mechanisms we elucidate). Transport measurements on semiconducting V_S- and Co-doped crystals then demonstrate complete mitigation of the internal junction, providing direct access to bulk electronic properties. We thereby report a host of previously inaccessible quantities and phenomena, including donor activation energies (down to 5 meV for Co), an unexpected second activated transport regime, electron mobility to 2100 $cm^2V^{-1}s^{-1}$, elucidation of very different mobilities in Co- and V_S-doped cases, and an abrupt T-dependent crossover to bulk Efros-Shklovskii variable-range hopping (ES VRH) [25] accompanied by an unusual non-linear Hall effect. Aspects of the results are interpreted *via* first-principles electronic structure calculations. Unequivocal mitigation of the internal *p-n* junction in pyrite single crystals is thus demonstrated, with implications for future fundamental studies and pyrite photovoltaic devices.

II. EXPERIMENTAL AND COMPUTATIONAL DETAILS

As discussed previously [10,11,16,26–28] and summarized in Supplemental Material Sec. A [29], high-quality pyrite single crystals (Fig. 1(b) inset) were grown by chemical vapor transport. Controlled doping with V_S or Co was achieved by S vapor pressure tuning during growth [10,16] and direct Co incorporation [10], respectively. The resulting crystals have been extensively characterized *via* powder X-ray diffraction, high-resolution single-crystal X-ray diffraction, X-ray rocking curves, energy dispersive X-ray spectroscopy, particle-induced X-ray emission, mass spectrometry, Raman spectroscopy, and atomic force microscopy [10,11,16,26–28]. Phase-pure, uniform, low defect density, low impurity concentration ($\leq$40 ppm metals basis, see ref. 16) crystals have been thus established [10,11,16,26–28].

Electronic transport measurement details are provided in Supplemental Material (Sec. B) [29]. Briefly, polished crystals [11] were used for all measurements, employing soldered In as a standard contact [10,16]. Alternatively, for CoS_2 contacts, ~30-nm-thick Co films were sputtered or evaporated on crystal surfaces (forming contact pads), then *ex situ* sulfidized for 8 h at 350 °C in a ~8 cm^3 quartz ampoule with 5 mg of S. As expected [20], this yields phase-pure metallic ferromagnetic CoS_2, with a volume expansion factor of ~3.85 (*i.e.*, CoS_2 thickness ~120 nm). X-ray diffraction (XRD) characterization of CoS_2 contact films was done on a Bruker D8 Discover diffractometer with a 2D detector, magnetic characterization was performed in a Quantum Design MPMS, and TOF-SIMS characterization of the CoS_2/FeS_2 interface was done in a PHI *nano*TOF II. Silver paint was used to contact the CoS_2 thin film pads, then four-wire van der Pauw measurements were made in DC and AC (16 Hz) modes, from 1.8 to 400 K in magnetic flux densities (B) up to 9 T.

As detailed in Supplemental Material [29], density functional theory (DFT) calculations were also performed to aid in the interpretation of some of the experimental results. These used the Vienna *ab initio* Simulation Package (VASP) [30–33], employing projected augmented wave pseudopotentials [34,35] and Perdew-Burke-Ernzerhof exchange-correlation functionals [36,37] with a Hubbard U correction [38]. All details, including the choice of U (for Fe and Co), are described in Supplemental Material [29]. Co- and V_S-doped FeS_2 were modeled in a 3 × 3 × 3 supercell containing one Co_{Fe} or a tetra-S-vacancy defect. The latter was found in recent work [17] to correspond most closely to experimental observations, highlighting the likely role of V_S clusters.

III. RESULTS AND DISCUSSION

Shown first in Figs. 1(b-d) are $\rho(T)$ data from crystals doped lightly with V_S (Fig. 1(b)), moderately with Co (Fig. 1(c)), and heavily with Co (Fig. 1(d)), *i.e.*, with increasing doping from top to bottom. Respective 300 K Hall electron densities [n(300 K)] are shown in each case, along with data taken with both In (dashed lines) and CoS_2 (solid lines) contacts. Starting at $n(300\ K) = 6 \times 10^{14}\ cm^{-3}$ (yellow, Fig. 1(b)), typical lightly-doped single-crystal FeS_2 behavior is observed [9–11,16], $\rho(T)$ first increasing upon cooling, then flattening at ~250 K, before rising again below ~50 K. As discussed above, this reflects freeze-out of the n-type interior as T is reduced from room temperature, followed by shunting by the more conductive heavily p-doped surface layer (see Fig. 1(a)) at low T [9–11,16]. (Thickness scaling, among other observations, confirmed low T surface conduction in prior work [9–11,16]). Increasing V_S doping to n(300 K) = 5 × 10^{16} cm^{-3} yields similar behavior, but with a bulk-to-surface conduction crossover at lower T (~100 K) due to lower bulk resistance. Significantly, in both of these cases the dashed and solid lines (In and CoS_2 contacts) are indistinguishable; low T current shunting by the exposed crystal surface between the contacts occurs regardless of the contact material. In the heaviest V_S-doped crystal in Fig. 1(b), however [n(300 K) = 1 × 10^{17} cm^{-3}], In and CoS_2 contacts generate strikingly different $\rho(T)$ at low T. [V_S] is now high enough to induce metalliclike, phonon-limited bulk $\rho(T)$ at high T (*i.e.*, $d\rho/dT > 0$), but, consistent with our recent report [10] and the above Introduction, $\rho(T)$ with In contacts shows an abrupt 10^4-fold increase below ~200 K. This reflects the equivalent circuit in the inset to Fig. 1(c), where the exponential rise of the p-n depletion region resistance on cooling (dictated by the ~300 meV junction barrier height) abruptly cuts off current to the crystal interior, restricting conduction to the surface layer only [10].

The n(300 K) = 1 × 10^{17} cm^{-3} $\rho(T)$ measured instead with CoS_2 contacts (Fig. 1(b), lowest solid line) provides a central result of this work. In stark contrast to the In contact case, no abrupt sub-200 K rise in $\rho(T)$ occurs, ρ being up to 10^4 times lower than with In. The resistivity instead gradually decreases down to ~100 K before rising to ~10^3 Ωcm at 1.8 K. *All characteristic $\rho(T)$ signatures of the internal p-n junction depletion region are thus entirely eliminated with ex-situ-sulfidized CoS_2 contacts, suggesting direct contact to the crystal interior*. This is indicated not only by the absence of the abrupt rise in $\rho(T)$ below ~200 K, but also the very low magnitude of the low T resistivity and resistance, far beneath anything associated with 2D surface conduction in FeS_2 crystals. These conclusions are further reinforced below by essentially all of the performed transport measurements. Fig. 1(c) shows that such behavior also occurs in moderately Co-doped crystals, the abrupt 125-175 K increase in $\rho(T)$ with In contacts being entirely extinguished with CoS_2 contacts. The increased doping here [up to $n(300\text{ K}) = 7 \times 10^{17}\text{ cm}^{-3}$] leads to quite weak $\rho(T)$ in CoS_2-contacted crystals, $\rho(T\rightarrow 0)$ in fact becoming finite. (A detailed study of the IMT with Co doping will be presented elsewhere [39]). The situation then changes at heavy Co doping [up to $n(300\text{ K}) = 3 \times 10^{18}\text{ cm}^{-3}$, Fig. 1(d)], where near-T-independent resistivity occurs, approaching 1 mΩcm. In this clearly metallic regime, $\rho(T)$ measured with In and CoS_2 contacts becomes essentially indistinguishable, again consistent with the equivalent circuit in the inset to Fig. 1(d). The n-doping is sufficiently high that the p-n depletion region becomes thin enough to permit ohmic contact to the crystal interior (likely *via* tunneling) [10,40], the low resistance metallic n-type bulk then dominating the p-type surface layer.

Figs. 1(b,c) thus demonstrate that at moderate doping, on the insulating side of the IMT, *i.e.,* in the range of interest for photovoltaics, the internal p-n junction in pyrite single crystals can be effectively mitigated with *ex situ* sulfidized CoS_2 contacts, providing direct access to bulk transport properties. In terms of establishing the *mechanism* of this mitigation, we first note, as described in Supplemental Material Sec. B (Fig. S1) [29], that subjecting FeS_2 crystals to the same S atmosphere thermal treatment *before* contact deposition does *not* lead to junction mitigation, highlighting the importance of thermal treatment of the Co/FeS_2 *interface*. Experiments were thus performed to verify CoS_2 formation and probe the depth profile of Co in the FeS_2 crystals after sulfidation (as depicted in Fig. 2(a)). As shown in the inset to Fig. 2(b), the conditions employed for *ex situ* sulfidation of Co overlayers [20] indeed result in single-phase

CoS_2 by XRD: the expected 200, 210, 211, and 220 reflections are observed, yielding a lattice parameter (5.54 Å) consistent with literature [19,20,41]. As further confirmation, the inset to Fig. 2(c) shows T-dependent magnetization data on such films, indicating $T_C \approx 120$ K, consistent with CoS_2 [18–20].

TOF-SIMS (see Supplemental Material Sec. C [29] for details, including Fig. S2) was then used to quantify Co depth profiles. Figs. 2(b,c) show depth profiles ($\log_{10}$ scale) of the TOF-SIMS intensity for Co^- and CoS_2^- secondary ions, respectively, for *ex situ* sulfidized CoS_2(120 nm)/FeS_2 contacts (maroon), and, for comparison, as-deposited Co(30 nm)/FeS_2 contacts (black). Examining the as-deposited Co/FeS_2 contacts first, as expected, we find a ~30 nm region above the interface (*i.e.*, negative depth in Fig. 2) with high Co^- and low CoS_2^- intensity. As sputtering proceeds into the FeS_2, the Co^- intensity drops ~10^3-fold within 100 nm (Fig. 2(b)), while the CoS_2^- signal (Fig. 2(c)) first rises abruptly (illustrating the sharpness of the Co/FeS_2 interface), before falling two orders-of-magnitude in 100 nm, *i.e.*, on the same approximate length scale as the Co^- decay. Importantly, this establishes baseline behavior for the apparent Co depth profile in FeS_2 crystals due to TOF-SIMS artifacts such as cascade mixing [42]. Moving to CoS_2 contacts, Figs. 2(b,c) first show the expected high Co^- and CoS_2^- intensities throughout the 120-nm-thick CoS_2 film (*i.e.*, at negative depth). More significantly, these intensities remain at or above this level to ~50 nm into the FeS_2. Both intensities then drop rapidly, with similar form to the as-deposited Co/FeS_2, *but with a distinct 30-50 nm shift to higher depths*. *Ex situ* sulfidation thus induces not only reaction of Co contacts to CoS_2 (Figs. 2(b,c) insets), but also clear CoS_2/FeS_2 interdiffusion (Figs. 2(a-c)), generating significant Co doping 30-50 nm into the FeS_2. In simple terms, a 10's of nm deep Co-doped n^+ region is thus generated under the CoS_2, yielding direct ohmic contact to the bulk, *via* mechanisms elucidated below.

Further quantification is provided by the solid orange lines through the CoS_2-contacted data in Figs. 2(b,c), which are fits to a 1D diffusion model, yielding a diffusion coefficient $D \approx 2 \times 10^{-16}$ cm^2s^{-1} (see Supplemental Material Sec. D [29] for details). $D(T)$ data for Co in FeS_2 are not available to our knowledge, but the similar ionic radii of Co^{2+} and Fe^{2+}, and full solubility in $Fe_{1-x}Co_xS_2$ [19,41], suggest similarity to Fe self-diffusion in FeS_2. $D \approx 8 \times 10^{-16}$ cm^2 s^{-1} at 350 °C for the latter [43], reassuringly close to our extracted value, verifying that the profiles in Fig. 2 are *quantitatively* consistent with expected diffusivities. As detailed in Supplemental Material Sec. D [29], an *n*-doping profile can then be constructed under simple assumptions, such as full dopant activation, accounting for detector saturation, and background effects. This is shown in Fig. S3 [29], indicating that doping as heavy as $n = 10^{20}$ cm^{-3} is maintained at up to 100 nm depth under CoS_2 contacts. Based on such information, Fig. 3 shows schematic illustrations of the situations realized directly under the contacts used here, thus elucidating the possible mechanisms for mitigation of the internal junction. Illustrated first in Fig. 3(a) is the situation with In contacts, showing the contact metal, heavily-doped *p*-type surface layer, depletion region, *n*-type bulk, and resulting band bending (as in Fig. 1(a)). One possibility for the situation under CoS_2 contacts is then illustrated in Fig. 3(b), which shows heavier doped (n^+) FeS_2 near the surface (due to in-diffusion of Co), thus shrinking the depletion region, narrowing the surface band bending region, and enabling tunneling from the CoS_2 metallic contact (and heavily-doped *p*-surface layer) to the *n*-FeS_2 bulk. This is a known mechanism for ohmic contacts to semiconductors [40]. Alternatively, and as illustrated in Fig. 3(c), the near-surface Co doping could be sufficiently heavy to (re)invert the *p*-surface, thereby realizing a direct *n*-CoS_2/*n*-FeS_2 interface and eliminating the internal *p-n* junction under the contact.

We emphasize two further points about these mechanisms. First, the schematics in Figs. 3(b,c) represent the situation in the immediate vicinity of the CoS_2 contacts only; the remainder of the macroscopic crystal is unaffected, enabling characterization of bulk transport properties of unperturbed bulk FeS_2 crystals. Second, the internal *p-n* junction mitigation demonstrated here is possible only due to: (*i*) the metallic nature of CoS_2 [19,20]; (*ii*) the fact that Co is a shallow donor in FeS_2 [10,21–24]; and (*iii*) the significant diffusivity of Co in FeS_2 at moderate temperatures [43]. Simpler thermal treatments such as vacuum annealing of Co contacts could *not* achieve this, due to the decomposition of the FeS_2 surface to pyrrhotite $Fe_{1-x}S$, which commences at as low as ~160 °C [26].

With CoS_2-contact-based mitigation of the internal *p-n* junction in FeS_2 crystals demonstrated, low T measurements of bulk transport properties of moderately doped semiconducting crystals become possible. We illustrate this in Fig. 4 by focusing on two representative crystals, one Co-doped (red, left panels) and one V_S-doped (green, right panels), both with $n(300\text{ K}) \approx 1 \times 10^{17}\text{ cm}^{-3}$, *i.e.*, in the doping range where low T bulk transport is normally obfuscated by the internal junction (Figs. 1(b,c)). Shown are the T dependence ($\log_{10}$ scale) of ρ (panels a,e), n (panels b,f), the apparent Hall mobility μ (panels c,g), and the 9 T perpendicular-to-plane magnetoresistance [$MR(9T) = (\rho(B) - \rho(0))/\rho(0)$] (panels d,h).

Focusing first on Co-doping (left panels), Fig. 4(a) shows that $\rho(T)$ is metalliclike on cooling from 400 K but then increases significantly between ~100 and 1.8 K, indicating transport on the insulating side of the IMT. This is consistent with the doping progression in CoS_2-contacted crystals in Figs. 1(b-d), and a thorough study of the IMT in FeS_2:Co [39], which places the critical electron density (n_c) at $\sim 2 \times 10^{17}\text{ cm}^{-3}$. Most noteworthy in Fig. 4(a) is the sharp slope discontinuity at ~20 K, marked with the dashed line. The origin of this is clarified by the

Zabrodskii plot [44] in the inset. Such plots display ln*W* *vs.* ln*T*, where $W = -d(\ln\rho)/d(\ln T)$, in order to linearize $\rho = \rho_0\exp(T_0/T)^m$, where $\rho_0 = \rho(T\rightarrow\infty)$, T_0 is a doping-dependent constant, and the exponent *m* reveals the semiconducting transport mechanism [44]. As illustrated by the solid line in the inset, the ~20 K feature marks an abrupt crossover from a regime where ln*W* decreases on cooling to a regime with $m \approx$ ½, corresponding to ES VRH [25]. As also shown in the ln ρ *vs.* $T^{-1/2}$ plot in Supplemental Material Sec. E, Fig. S4(a) [29], the $m \approx$ ½ regime spans ~20 to 1.8 K (*i.e.*, an order of magnitude in *T*), and two orders of magnitude in ρ, thus establishing ES VRH with confidence. The extracted T_0 = 65 K is quite low [25], indicating relative proximity to the IMT, consistent with $n/n_c \approx 0.5$. The data of Fig. 4(a) thus indicate an abrupt *T*-dependent bulk crossover from diffusive to hopping transport at cryogenic temperatures. This demonstrates that state-of-the-art pyrite single crystals exhibit bulk behavior strikingly reminiscent of prototypical doped semiconductors such as Ge [25,45].

As seen in Fig. 4(b), the diffusive to hopping crossover is yet more conspicuous in *n*(*T*). As illustrated by the solid line fit and Arrhenius plot in Supplemental Material Sec. F (Fig. S5(a)) [29], activated behavior occurs above ~20 K, with an activation energy ΔE = 4.9 meV. Importantly, due to the prior inability to probe bulk transport below ~100-200 K, and the low ΔE for Co, there are no literature values to compare this to. Comparison to donor ionization energies from the hydrogenic model is possible, however. While uncertainties exist with respect to the effective mass and dielectric constant in FeS_2, the best available values of $m_e^* \approx 0.5m_e$ [17,46,47] and $\varepsilon_r \approx 20$ [48] yield a ~16 meV donor ionization energy. This is not inconsistent with our observation, the measured ΔE = 4.9 meV potentially being decreased from the ~16 meV non-interacting donor ionization energy due to approach to the IMT ($n/n_c \approx 0.5$ here) [25,45]. We note as an aside that such values are distinctly lower than the 90 meV inferred from optical absorption [24], highlighting the importance of bulk transport characterization. Returning to Fig. 4(b), as T is lowered from the diffusive to hopping regime, below ~20 K, a dramatic *apparent* increase in n occurs. This reflects the well-known suppression of the Hall coefficient in hopping transport [27,49–52], however, Fig. 4(b) thus being qualitatively consistent with Fig. 4(a). As expected, based on the above, there is no evidence of an n-type bulk to p-type surface crossover (as with conventional contacts) but rather a bulk n-type diffusive to hopping crossover (not previously accessible).

Fig. 4(c) shows the resulting Hall mobility, μ. Classic moderately doped semiconducting behavior occurs, μ first increasing on cooling in a phonon-scattering-limited regime, before decreasing in an ionized-impurity-limited regime [40]. A peak mobility of 200 $\mathrm{cm^2V^{-1}s^{-1}}$ is attained at 150 K. The solid line in Fig. 4(c) is a fit to a simplified model describing both regimes with power laws and using Matthiessen's rule (additive scattering rates) to write $\left(\mu(T)\right)^{-1} = (aT^{-\alpha})^{-1} + (bT^{\beta})^{-1}$, where α and β describe phonon and ionized impurity scattering, respectively (a and b are constants) [40]. A good fit is obtained over the entire diffusive transport regime ($20 < T < 400$ K), yielding reasonable values of $\alpha = 1.2$ and $\beta = 2.2$. More significantly, at ~20 K the apparent mobility begins to abruptly drop (due to the apparent rise in n from Hall coefficient suppression), right at $\mu \approx 1$ $\mathrm{cm^2V^{-1}s^{-1}}$. The previously inaccessible bulk hopping to diffusive crossover thus occurs very close to the generic ~1 $\mathrm{cm^2V^{-1}s^{-1}}$ often touted as an approximate threshold for diffusive band transport [27,53,54].

Fig. 4(d) then shows the T-dependent MR ratio in a 9 T perpendicular field. At $T > 20$ K, classic ordinary MR is observed, with positive sign, parabolic B dependence, and MR(T) (Fig. 4(d)) that tracks μ(T) (Fig. 4(c)) (see Supplemental Material Sec. G, Figs. S6 and S7 [29], for details). Below 20 K, the positive MR then abruptly increases. As shown in the inset to Fig. 4(d), ln[ρ(B)/ρ(0)] at these lowest T exhibits parabolic B dependence (solid line fit), characteristic of the field-induced wave-function overlap decrease in ES-VRH [25]. The localization length L_c can then be extracted using $\ln\left(\frac{\rho(B)}{\rho(0)}\right) = \frac{s}{\hbar^2} {L_c}^4 B^2 \left(\frac{T_0}{T}\right)^{3/2}$ [25], where s is a dimensionless constant (0.0015), $\hbar$ is the reduced Planck constant, and T_0 = 65 K is known from ρ(T) (Figs. 4(a) and S4(a) [29]). This yields L_c = 13 nm, expanded significantly over the hydrogenic Bohr radius (~2.5 nm, subject to the same uncertainties as the donor ionization energy), again consistent with approaching the IMT ($n/n_c \approx 0.5$) [25,45]. Fig. 4(d) thus establishes MR quantitatively consistent with a bulk diffusive to hopping crossover at ~20 K, in accord with ρ(T), n(T), and μ(T) (Figs. 4(a-c)).

Moving to V_S doping (green, right panels), Fig. 4(e) reveals a similar situation to Fig. 4(a) but with slightly lower ρ at low T and a slightly lower crossover temperature of ~12 K (vertical dashed line). Consequently, ES VRH is more difficult to establish definitively, but m = 0.5 does describe the low T data in the inset to Fig. 4(e), consistent with ln ρ *vs*. $T^{1/2}$ (Supplemental Material Sec. E, Fig. S4(b) [29]). A low T_0 of ~35 K is thus determined, indicating closer proximity to the IMT than the Co-doped sample, likely due to slightly higher doping. Significantly, CoS_2 contacts now enable us to fully explore the bulk n(T) (Fig. 4(f)), for which prior work (which was limited to higher T by the internal p-n junction) hinted at the possibility of two distinct activation energies in FeS_2:V_S [10,16]. As illustrated by the solid line fits in Fig. 4(f) and the Arrhenius plots in Fig. S5(b), two activated regimes indeed occur. At the highest T (>325 K), ΔE_1 = 56 meV, while ΔE_2 = 6.4 meV describes the 12 K < T < 325 K data. ΔE_1 is consistent with earlier high T measurements of V_S-doped FeS_2 crystals, which revealed a ΔE that gradually drops from the ~225 meV limiting value at light doping (the deep donor ionization energy) to

~17 meV at the heaviest V_S doping achieved [10,16]. As already noted [16], this approach to the IMT due to doping with such a deep donor is very different from the better-understood approach to the IMT with shallow donors and can now be studied to low T in V_S-doped pyrite. Although multiple activation energies and levels in the gap are known in certain semiconductors [40], the specific origin of the two distinct ΔE values here is unclear. In this regard, note that: (*i*) we do not believe that ΔE_2 is simply related to background Co impurities in V_S-doped crystals [16] as ΔE_2 is not observed at all V_S doping levels; (*ii*) just like ΔE_1, ΔE_2 collapses on approaching the IMT, from ~25 meV at n(300 K) = 8 × 10^{16} cm^{-3} [10] to 6.4 meV at n(300 K) ≈ 1 × 10^{17} cm^{-3}; (*iii*) in light of recent theoretical work [17], it is plausible that distinct types of V_S clusters and/or V_S interactions could produce multiple ΔE. Further work will be required to resolve this, enabled by the internal junction mitigation demonstrated here. Regardless, cooling below ~12 K in Fig. 4(f) induces the same type of rapid increase in apparent n as in Fig. 4(b), again reflecting the suppression of the Hall coefficient in the hopping regime [27,49–52].

Turning to mobility in the V_S-doped case, Fig. 4(g) again reveals a peak at intermediate T, this time reaching 2100 $cm^2V^{-1}s^{-1}$ at 75 K. Significantly, this can be compared to peak mobilities of 2000 $cm^2V^{-1}s^{-1}$ in Schieck *et al.* [55], 1930 $cm^2V^{-1}s^{-1}$ in Limpinsel *et al.* [9], and ~800 $cm^2V^{-1}s^{-1}$ in Tomm *et al.* [56], demonstrating outstanding mobility. $\mu(T)$ is again described by $(\mu(T))^{-1} = (aT^{-\alpha})^{-1} + (bT^{\beta})^{-1}$ across the entire diffusive regime (12 - 400 K), yielding α = 2.6 and β = 0.89. The broad range of phonon-limited transport here (75 - 400 K, enabled by the mitigation of the internal *p-n* junction) in fact allows for more accurate determination of α than the Co-doped case, α = 2.6 being in good agreement with several higher T FeS_2 studies [9,11,56]. Analogous to Co doping, and in accord with Figs. 4(e,f), the apparent $\mu(T)$ then abruptly drops at the ~12 K crossover to hopping transport.

The higher mobility in V_S-doped crystals, which we observe over the entire doping range, is particularly noteworthy. This amounts to as much as a factor of 10 in peak mobility between V_S- and Co-doping in Figs. 4(c,g) (2100 $cm^2V^{-1}s^{-1}$ *cf.* 200 $cm^2V^{-1}s^{-1}$), surely related to the rather different nature of the dopants. This is illustrated in Figs. 5(a,b), where DFT band structures and spin-resolved densities-of-states (DOS) are compared for Co- and V_S-doped pyrite. These figures show the expected ~0.95-eV-band-gap, the conduction band minimum being dominated by dispersive S 3*p* states [17]. As shown in Fig. 5(a), Co doping introduces a narrow band of defect states close to the conduction band minimum [57,58] (at ~0.95 eV in the left panel), corresponding to the small (spin-split) DOS peak in the right panel. As would be expected, the Fermi energy (green line) is then very close to the conduction band minimum. It should be noted, as discussed in Supplemental Material Sec. H (including Figs. S8 and S9) [29], that such results depend on the value of U for Co. Low U on Co (*e.g.*, 2 eV) results in delocalized electrons populating the S 3*p* conduction band, high U on Co (*e.g.*, 4 eV) results in a localized donor state ~100 meV below the conduction band minimum, and U = 3 eV (as in Fig. 5(a)) results in a shallow donor state. The latter is clearly most consistent with experiment, and we thus focus on this case. Notably different is the V_S-doped case (Fig. 5(b)), which, based on prior work [17], was modeled with a tetra-S-vacancy generating a deep donor state. As shown in Fig. 5(b), the Fermi energy thus lies in the gap in these 3 × 3 × 3 supercell calculations, the S-3*p*-dominated conduction band being essentially unaffected. Comparison of Figs. 5(a,b) then provides a simple potential qualitative explanation for the higher electron mobilities in semiconducting V_S-doped FeS_2 *cf.* Co-doped FeS_2. The former has essentially unperturbed dispersive S 3*p* states in the conduction band, while Co doping generates a narrow band of states very close to the conduction band minimum, likely negatively impacting both m_e^* and the electron-phonon scattering rate (through the increased DOS). Local magnetic moments on the Co dopants could yield yet more scattering, further decreasing the mobility.

Returning to Fig. 4 to complete the discussion of FeS_2:V_S transport, Fig. 4(h) shows that the MR in V_S-doped crystals is similar to FeS_2:Co, again exhibiting the prototypical crossover from positive, parabolic, mobility-tracking ordinary MR in the diffusive regime (>12 K) to ES VRH MR at <12 K. The fit in the inset to Fig. 4(h) yields L_c = 16 nm, slightly larger than the 13 nm from Fig. 4(d), consistent with the lower T_0. Interestingly, as shown in Supplemental Material Sec. G [29], some evidence of sub-parabolic B dependence emerges at intermediate T (*e.g.*, 75 K, Fig. S6(d) [29]). As will be discussed elsewhere [39], a significant regime of near-B-linear positive MR can also be found in certain T and doping regimes in Co-doped FeS_2 crystals, another unexpected finding enabled by access to low T bulk transport.

As a final point, we emphasize that the results in Figs. 4(b,c,f,g) are based on low $|B|$ (<1 T) Hall measurements. At higher $|B|$, an interesting non-linear Hall effect emerges, as shown in Fig. 6. The insets to Figs. 6(a,b) illustrate this effect in Co- and V_S-doped crystals, showing that the transverse (Hall) resistance (R_{xy}) is non-linear in B. dR_{xy}/dB evolves from a maximum at low $|B|$ to a smaller value at high $|B|$, which we simply quantify by extracting two apparent Hall densities, n_L (at $|B| \leq 1$ T) and n_H (at $|B| \geq 7$ T), as illustrated in the insets (dashed black lines). The ratio n_H/n_L is then plotted *vs*. T in Figs. 6(a,b), revealing gradual rises in non-linearity (*i.e.*, $n_H/n_L > 1$) on cooling below ~200 K, maxima close to the crossovers to hopping (~20 and ~12 K for Co and V_S doping), then rapid decreases as the Hall coefficient is suppressed in the hopping regime. Notably, the peak n_H/n_L is around twice as large for the higher mobility V_S-doped case than the Co-doped case. Generally, such Hall non-linearity reflects multiple carrier populations, such as electrons and holes [59–61], multiple bands [62–64], bulk and surface channels [9,11,60,61,65] (as in lightly doped FeS_2 [9,11]), *etc*. We have definitively established bulk transport here, however, and the non-linear Hall effect accompanying the *n*-type bulk to *p*-type surface crossover in conventionally-contacted FeS_2 crystals is very different from Fig. 6. The only obvious possibilities for distinct transport contributions are thus from diffusive and hopping channels (due to inhomogeneity on the approach to the IMT, for example) or distinct donor states/donor bands in the gap, as discussed above in light of two activation energies and different mobilities in the V_S- and Co-doped cases. Further analysis along these lines is hindered by the absence of a theory of the Hall effect for coexisting diffusive and hopping channels, and uncertainties regarding the origin of the multiple activation energies. Further work will be required to clarify this, enabled by the access to low *T* bulk transport properties provided by the internal junction mitigation demonstrated here. The observations in Fig. 6 are in fact a clear illustration of the many transport phenomena in doped FeS_2 previously obfuscated by the internal junction.

IV. SUMMARY AND DISCUSSION

In summary, careful *T*-dependent transport measurements and analyses have been coupled with XRD and magnetometry characterization, and TOF-SIMS depth profiling, to establish complete mitigation of the internal *p-n* junction in CoS_2-contacted FeS_2 single crystals. The metallicity of CoS_2 [18,19], shallow donor nature of Co [10, 21-24, 66], and significant diffusivity of Co in FeS_2 [43] are simultaneously exploited to produce metallic CoS_2 contacts that also induce heavy diffusion doping of FeS_2 to 10's of nm depths, generating direct ohmic contact to the crystal interior [*via* mechanisms we have discussed (Fig. 3)]. This enables previously inaccessible *bulk* transport studies of moderately doped semiconducting FeS_2, elucidating activation energies, multiple regimes of activated transport, electron mobilities up to

2100 cm^{2}V^{-1}s^{-1}, very different mobilities in Co- and V_S-doped cases, an abrupt T-dependent crossover from diffusive to hopping transport (strikingly reminiscent of prototypical doped semiconductors), and an unusual non-linear Hall effect near the diffusive to hopping crossover. Such diffused CoS_2 contacts can now be tactically employed in future work, both for fundamental studies and for further development of pyrite-based photovoltaics.

In terms of implications of our findings from fundamental and applied (*e.g.*, photovoltaic) perspectives, we wish to emphasize some key points. In terms of fundamental knowledge, the access to low T bulk transport measurements provided here already elucidates very different donor level positions in Co- and V_S-doped cases, highlighting that further work is required to understand the two activation energies in V_S-doped FeS_2 and that Co indeed appears to be an ideal shallow donor. The order-of-magnitude lower peak mobility for Co doping (which we explain *via* the calculations presented in Fig. 5) was not anticipated, however, highlighting the desirability of doping beyond the IMT with V_S. In particular, the high mobilities in that case could enable quantum transport measurements (*e.g.*, of Shubnikov-de Haas oscillations), providing valuable fundamental information, including more accurate m_e^* values; uncertainties due to the latter were noted several times above. Our findings also illustrate that further magnetotransport studies should be performed on FeS_2 crystals, exploring both the near-B-linear MR (which is of high general interest [67]) and the non-linear Hall effect shown in Fig. 6. More generally, the results of Fig. 4 establish that state-of-the-art doped-FeS_2 single crystals are of sufficient electronic quality to enable detailed studies of both diffusive to hopping and insulator to metal transitions.

In terms of implications of our work for *applications* of pyrite, particularly in photovoltaic devices, we first note that ohmic CoS_2-based contacts of the type established here are of clear utility for back contacts in solar cells. Back CoS_2 contacts paired with conventional top contacts could also enable *vertical*-transport-based characterization of the internal *p-n* junction in pyrite crystals (a significant step beyond prior work [10]), including voltage-dependent characterization. The latter would constitute a first step to potentially understanding and harnessing the naturally-formed internal FeS_2 *p-n* junction for photovoltaic purposes. Wide-*T*-range measurements of Hall electron and hole densities could also now enable further understanding of donor and acceptor levels. The results here already demonstrate how different these are for Co and V_S donors and open up the determination of equivalent energies for potential acceptors. The latter are poorly established in pyrite, even though *p-n* homojunction devices offer a novel route to pyrite solar cells, potentially side-stepping issues with surface states. It has also been noted [7,9] that the deep donor nature of V_S in pyrite could limit V_{OC} in heterojunction devices, related to the band bending shown in Figs. 1(a) and 3. The current work establishes a means to assess $n(T)$ over a broad T range in FeS_2 single crystals, thus reliably determining V_S-related donor levels, a prerequisite for controlling either the concentration or donor level position of V_S in FeS_2.

ACKNOWLEDGMENTS: Work supported by the customers of Xcel Energy through the Renewables Development Fund, and in part by the National Science Foundation NSF through the University of Minnesota (UMN) MRSEC under DMR-2011401. Work on Co-doped FeS_2 specifically was supported by the US Department of Energy through the UMN Center for Quantum Materials under DE-SC-0016371. Parts of this work were carried out in the Characterization Facility, UMN, which receives partial support from NSF through the MRSEC program. B.V. acknowledges the UMN Doctoral Dissertation Fellowship and D.R. acknowledges the Minnesota Supercomputing Institute for computing resources. We thank B.

Shklovskii and T. Birol for informative discussions, and J. Batley for Co contact evaporation and discussions.

REFERENCES

[1] C. Wadia, A. P. Alivisatos, and D. M. Kammen, Materials availability expands the opportunity for large-scale photovoltaics deployment, Environ. Sci. Technol. **43**, 2072 (2009).

[2] A. Ennaoui, S. Fiechter, C. Pettenkofer, N. Alonso-Vante, K. Büker, M. Bronold, C. Höpfner, and H. Tributsch, Iron disulfide for solar energy conversion, Sol. Energy Mater. Sol. Cells **29**, 289 (1993).

[3] A. Ennaoui and H. Tributsch, Iron sulphide solar cells, Sol. Cells **13**, 197 (1984).

[4] A. Ennaoui and H. Tributsch, Energetic characterization of the photoactive FeS_2 (pyrite) interface, Sol. Energy Mater. **14**, 461 (1986).

[5] A. Ennaoui, S. Fiechter, W. Jaegermann, and H. Tributsch, Photoelectrochemistry of highly quantum efficient single-crystalline n-FeS_2 (pyrite), J. Electrochem. Soc. **133**, 97 (1986).

[6] K. Büker, N. Alonso-Vante, and H. Tributsch, Photovoltaic output limitation of n-FeS_2 (pyrite) Schottky barriers: A temperature-dependent characterization, J. Appl. Phys. **72**, 5721 (1992).

[7] M. Cabán-Acevedo, N. S. Kaiser, C. R. English, D. Liang, B. J. Thompson, H. Chen, K. J. Czech, J. C. Wright, R. J. Hamers, and S. Jin, Ionization of high-density deep donor defect states explains the low photovoltage of iron pyrite single crystals, J. Am. Chem. Soc. **136**, 17163 (2014).

[8] D. Liang, M. Cabán-Acevedo, N. S. Kaiser, and S. Jin, Gated hall effect of nanoplate devices reveals surface-state-induced surface inversion in iron pyrite semiconductor, Nano Lett. **14**, 6754 (2014).

[9] M. Limpinsel, N. Farhi, N. Berry, J. Lindemuth, C. L. Perkins, Q. Lin, and M. Law, An inversion layer at the surface of n-type iron pyrite, Energy Environ. Sci. **7**, 1974 (2014).

[10] B. Voigt, W. Moore, M. Maiti, J. Walter, B. Das, M. Manno, C. Leighton, and E. S. Aydil, Observation of an internal $p{-}n$ junction in pyrite FeS_2 single crystals: Potential origin of the low open circuit voltage in pyrite solar cells, ACS Mater. Lett. **2**, 861 (2020).

[11] J. Walter, X. Zhang, B. Voigt, R. Hool, M. Manno, F. Mork, E. S. Aydil, and C. Leighton, Surface conduction in n-type pyrite FeS_2 single crystals, Phys. Rev. Mater. **1**, 065403 (2017).

[12] M. Bronold, K. Buker, S. Kubala, C. Pettenkofer, and H. Tributsch, Surface Preparation of FeS_2 *via* electrochemical etching and interface formation with metals, Phys. Status Solidi **135**, 231 (1993).

[13] M. Bronold, Y. Tomm, and W. Jaegermann, Surface states on cubic d-band semiconductor pyrite (FeS_2), Surf. Sci. **314**, L931 (1994).

[14] R. Murphy and D. R. Strongin, Surface reactivity of pyrite and related sulfides, Surf. Sci. Rep. **64**, 1 (2009).

[15] F. W. Herbert, A. Krishnamoorthy, W. Ma, K. J. Van Vliet, and B. Yildiz, Dynamics of point defect formation, clustering and pit initiation on the pyrite surface, Electrochim. Acta **127**, 416 (2014).

[16] B. Voigt, W. Moore, M. Manno, J. Walter, J. D. Jeremiason, E. S. Aydil, and C. Leighton, Transport evidence for sulfur vacancies as the origin of unintentional n-type doping in pyrite FeS_2, ACS Appl. Mater. Interfaces **11**, 15552 (2019).

[17] D. Ray, B. Voigt, M. Manno, C. Leighton, E. S. Aydil, and L. Gagliardi, Sulfur vacancy clustering and its impact on electronic properties in pyrite FeS_2, Chem. Mater. **32**, 4820

(2020).
[18] H. Hiraka and Y. Endoh, Ferromagnetic transition of Heisenberg ferromagnetic metal of CoS_2 - Static critical properties, J. Phys. Soc. Japan **63**, 4573 (1994).
[19] C. Leighton, M. Manno, A. Cady, J. W. Freeland, L. Wang, K. Umemoto, R. M. Wentzcovitch, T. Y. Chen, C. L. Chien, P. L. Kuhns, M. J. R. Hoch, A. P. Reyes, W. G. Moulton, E. D. Dahlberg, J. Checkelsky, and J. Eckert, Composition controlled spin polarization in $Co_{1-x}Fe_xS_2$ alloys, J. Phys. Condens. Matter **19**, 315219 (2007).
[20] M. Manno, R. Frakie, and C. Leighton, Synthesis and characterization of highly spin-polarized single-phase $Co_{1-x}Fe_xS_2$ films, J. Appl. Phys. **105**, 093912 (2009).
[21] S. W. Lehner, K. S. Savage, and J. C. Ayers, Vapor growth and characterization of pyrite (FeS_2) doped with Co, Ni, and As: Variations in semiconducting properties, J. Cryst. Growth **286**, 306 (2006).
[22] S. Guo, D. P. Young, R. T. Macaluso, D. A. Browne, N. L. Henderson, J. Y. Chan, L. L. Henry, and J. F. Ditusa, Discovery of the Griffiths Phase in the Itinerant Magnetic Semiconductor $Fe_{1-x}Co_xS_2$, Phys. Rev. Lett. **100**, 017209 (2008).
[23] S. Guo, D. P. Young, R. T. Macaluso, D. A. Browne, N. L. Henderson, J. Y. Chan, L. L. Henry, and J. F. Ditusa, Charge transport in cobalt-doped iron pyrite, Phys. Rev. B **81**, 144424 (2010).
[24] S. W. Lehner, N. Newman, M. Van Schilfgaarde, S. Bandyopadhyay, K. Savage, and P. R. Buseck, Defect energy levels and electronic behavior of Ni-, Co-, and As-doped synthetic pyrite (FeS_2), J. Appl. Phys. **111**, 083717 (2012).
[25] B. I. Shklovskii and A. L. Efros, *Electronic Properties of Doped Semiconductors* (Springer, Berlin, 1984).
[26] X. Zhang, T. Scott, T. Socha, D. Nielsen, M. Manno, M. Johnson, Y. Yan, Y. Losovyj, P. Dowben, E. S. Aydil, and C. Leighton, Phase stability and stoichiometry in thin film iron pyrite: Impact on electronic transport properties, ACS Appl. Mater. Interfaces **7**, 14130 (2015).
[27] X. Zhang, M. Li, J. Walter, L. O’Brien, M. A. Manno, B. Voigt, F. Mork, S. V. Baryshev, J. Kakalios, E. S. Aydil, and C. Leighton, Potential resolution to the doping puzzle in iron pyrite: Carrier type determination by Hall effect and thermopower, Phys. Rev. Mater. **1**, 015402 (2017).
[28] J. Walter, B. Voigt, E. Day-Roberts, K. Heltemes, R. M. Fernandes, T. Birol, and C. Leighton, Voltage-induced ferromagnetism in a diamagnet, Sci. Adv. **6**, eabb7721 (2020).
[29] See Supplemental Material at www.aps.org/xxxx, (2020).
[30] G. Kresse and J. Hafner, Ab initio molecular dynamics for liquid metals, Phys. Rev. B **47**, 558 (1993).
[31] G. Kresse and J. Hafner, Ab initio molecular-dynamics simulation of the liquid-metal–amorphous-semiconductor transition in germanium, Phys. Rev. B **49**, 14251 (1994).
[32] G. Kresse and J. Furthmüller, Efficient iterative schemes for ab initio total-energy calculations using a plane-wave basis set, Phys. Rev. B **54**, 11169 (1996).
[33] G. Kresse and J. Furthmüller, Efficiency of ab-initio total energy calculations for metals and semiconductors using a plane-wave basis set, Comput. Mater. Sci. **6**, 15 (1996).
[34] P. E. Blöchl, Projector augmented-wave method, Phys. Rev. B **50**, 17953 (1994).
[35] G. Kresse, From ultrasoft pseudopotentials to the projector augmented-wave method, Phys. Rev. B **59**, 1758 (1999).
[36] J. P. Perdew and Y. Wang, Accurate and simple analytic representation of the electron-gas

correlation energy, Phys. Rev. B **45**, 13244 (1992).

[37] J. P. Perdew, K. Burke, and M. Ernzerhof, Generalized gradient approximation made simple, Phys. Rev. Lett. **77**, 3865 (1996).

[38] A. Rohrbach, J. Hafner, and G. Kresse, Electronic correlation effects in transition-metal sulfides, J. Phys. Condens. Matter **15**, 979 (2003).

[39] B. Das, B. Voigt, M. Maiti, M. Manno, E. S. Aydil, and C. Leighton, Insulator-metal transition in Co-doped pyrite single crystals, in preparation.

[40] S. M. Sze, *Physics of Semiconductor Devices* (John Wiley & Sons, New York, 1981).

[41] T. Kinner, K. P. Bhandari, E. Bastola, B. M. Monahan, N. O. Haugen, P. J. Roland, T. P. Bigioni, and R. J. Ellingson, Majority carrier type control of cobalt iron sulfide ($Co_xFe_{1-x}S_2$) pyrite nanocrystals, J. Phys. Chem. C **120**, 5706 (2016).

[42] P. Williams and J. E. Baker, Quantitative analysis of interfacial impurities using secondary-ion mass spectrometry, Appl. Phys. Lett. **36**, 842 (1980).

[43] J. H. Chen and W. W. Harvey, Cation self-diffusion in chalcopyrite and pyrite, Metall. Trans. B **6B**, 331 (1975).

[44] A. G. Zabrodskii, The Coulomb gap: The view of an experimenter, Philos. Mag. B **81**, 1131 (2001).

[45] N. Mott, *Metal-Insulator Transitions*, 2nd ed. (Taylor & Francis, London, 1990).

[46] A. M. Karguppikar and A. G. Vedeshwar, Transport properties of thin iron pyrite films, Phys. Status Solidi **95**, 717 (1986).

[47] J. Hu, Y. Zhang, M. Law, and R. Wu, First-principles studies of the electronic properties of native and substitutional anionic defects in bulk iron pyrite, Phys. Rev. B **85**, 085203 (2012).

[48] S. G. Choi, J. Hu, L. S. Abdallah, M. Limpinsel, Y. N. Zhang, S. Zollner, R. Q. Wu, and M. Law, Pseudodielectric function and critical-point energies of iron pyrite, Phys. Rev. B **86**, 115207 (2012).

[49] L. Friedman, Hall conductivity of amorphous semiconductors in the random phase model, J. Non. Cryst. Solids **6**, 329 (1971).

[50] P. G. Le Comber, D. I. Jones, and W. E. Spear, Hall effect and impurity conduction in substitutionally doped amorphous silicon, Philos. Mag. A **35**, 1173 (1977).

[51] J. Kakalios, A physical interpretation of the Hall effect in amorphous semiconductors, J. Non. Cryst. Solids **114**, 372 (1989).

[52] Y. M. Gal'perin, E. P. German, and V. G. Karpov, Hall effect under hopping conditions, Zh. Eksp. Teor. Fiz. **99**, 343 (1991).

[53] S. Stafström, Electron localization and the transition from adiabatic to nonadiabatic charge transport in organic conductors, Chem. Soc. Rev. **39**, 2484 (2010).

[54] S. Wang, M. Ha, M. Manno, C. D. Frisbie, and C. Leighton, Hopping transport and the Hall effect near the insulator-metal transition in electrochemically gated poly(3-hexylthiophene) transistors, Nat. Commun. **3**, 1210 (2012).

[55] R. Schieck, A. Hartmann, S. Fiechter, R. Könenkamp, and H. Wetzel, Electrical properties of natural and synthetic pyrite (FeS_2) crystals, J. Mater. Res. **5**, 1567 (1990).

[56] Y. Tomm, R. Schieck, K. Ellmer, and S. Fiechter, Growth mechanism and electronic properties of doped pyrite (FeS_2) crystals, J. Cryst. Growth **146**, 271 (1995).

[57] P. Lazi, R. Armiento, F. W. Herbert, R. Chakraborty, R. Sun, M. K. Y. Chan, K. Hartman, T. Buonassisi, B. Yildiz, and G. Ceder, Low intensity conduction states in FeS_2: Implications for absorption, open-circuit voltage and surface recombination, J. Phys.

Condens. Matter **25**, 465801 (2013).

[58] E. Day-Roberts, T. Birol, and R. M. Fernandes, Contrasting ferromagnetism in pyrite FeS_2 induced by chemical doping versus electrostatic gating, Phys. Rev. Mater. **4**, 054405 (2020).

[59] N. P. Armitage, E. J. Mele, and A. Vishwanath, Weyl and Dirac semimetals in three-dimensional solids, Rev. Mod. Phys. **90**, 015001 (2018).

[60] M. Z. Hasan and C. L. Kane, Colloquium: Topological insulators, Rev. Mod. Phys. **82**, 3045 (2010).

[61] X. L. Qi and S. C. Zhang, Topological insulators and superconductors, Rev. Mod. Phys. **83**, 1057 (2011).

[62] H. Yang, Y. Liu, C. Zhuang, J. Shi, Y. Yao, S. Massidda, M. Monni, Y. Jia, X. Xi, Q. Li, Z. K. Liu, Q. Feng, and H. H. Wen, Fully band-resolved scattering rate in MgB_2 revealed by the nonlinear Hall effect and magnetoresistance measurements, Phys. Rev. Lett. **101**, 067001 (2008).

[63] S. Stemmer and S. James Allen, Two-dimensional electron gases at complex oxide interfaces, Annu. Rev. Mater. Res. **44**, 151 (2014).

[64] J. A. Sulpizio, S. Ilani, P. Irvin, and J. Levy, Nanoscale phenomena in oxide heterostructures, Annu. Rev. Mater. Res. **44**, 117 (2014).

[65] H. Wang, J. Walter, K. Ganguly, B. Yu, G. Yu, Z. Zhang, H. Zhou, H. Fu, M. Greven, and C. Leighton, Wide-voltage-window reversible control of electronic transport in electrolyte-gated epitaxial $BaSnO_3$, Phys. Rev. Mater. **3**, 075001 (2019).

[66] R. N. Chandler, R. W. Bené, EPR study of the solid solutions $Ni_xFe_{1-x}S_2$, $Co_xFe_{1-x}S_2$, and $Co_xNi_yFe_{1-x-y}S_2$, Phys. Rev. B. **8**, 4979-4988 (1977).

[67] J. Singleton, Temperature scaling behavior of the linear magnetoresistance observed in high-temperature superconductors, Phys. Rev. Mater. **4**, 061801(R) (2020).

FIGURE CAPTIONS

Figure 1. (a) Schematic band diagram of an *n*-FeS_2 crystal (with the surface on the extreme left). Shown are the conduction band (E_C), valence band (E_V), and Fermi (E_F) energies, along with the *n*-bulk, *p*-*n* depletion, and *p*-surface regions. Note the substantial upward band bending towards the surface. For scale, the accepted energy gap in FeS_2 is ~0.95 eV. Temperature (T) dependence of the resistivity (ρ) of FeS_2 single crystals with (a) light S vacancy (V_S) doping [n(300 K) = 6×10^{14}, 5×10^{15}, 1×10^{17} cm^{-3}], (b) moderate Co doping [n(300 K) = 3×10^{17}, 7×10^{17} cm^{-3}], and (c) heavy Co doping [n(300 K) = 1×10^{18}, 3×10^{18} cm^{-3}]. [n(300 K) is the 300 K Hall electron density]. Data are shown for both In contacts (dashed lines) and CoS_2 contacts (solid lines). A typical crystal is shown in (a) (adapted with permission from ref. 16. Copyright 2019 American Chemical Society). The insets to (b) and (c) are schematics (not to scale) showing the *n*-type bulk (dark blue), *p*-type surface (red), *p*-*n* depletion region (light blue), and equivalent circuit diagrams. Note that due to heavy doping in the *p*-type surface layer, the depletion width is controlled by the *n*-doping in the crystal interior.

Figure 2. (a) Schematic composition profile of a CoS_2-contacted FeS_2 crystal. Time-of-flight secondary ion mass spectrometry (TOF-SIMS) depth profiles ($\log_{10}$ scale) of (b) Co^- and (c) CoS_2^- through the interface of an FeS_2 crystal contacted with ~120 nm of sulfidized CoS_2 (maroon); for reference, data for ~30 nm as-deposited Co contacts are also shown (black). Orange lines represent a 1D diffusion model with diffusivity $D \approx 2 \times 10^{-16}$ cm^2s^{-1} (see Supplemental Material Sec. D [29] for details). The insets to (b,c) show an XRD pattern (intensity (I) *vs*. 2θ) and magnetization (M) *vs*. temperature (T) for representative 120-240-nm-

thick CoS_2 films. Expected CoS_2 reflections [19,20,41] are marked; the peak near 30.5° likely arises from the sample holder. $M(T)$ was measured in 500 Oe after field-cooling in 500 Oe.

Figure 3. Schematic illustrations and band diagrams directly under contacts formed with (a) conventional In and (b,c) interdiffused CoS_2. The *n*-bulk, *p*-*n* depletion regions, *p*-surface regions, and contact layers are shown, along with the conduction band (E_C), valence band (E_V), and Fermi (E_F) energies. The different scenarios in (b) and (c) correspond to shrinking of the depletion region to the point of tunneling and direct (re)inversion of the *p*-surface layer, respectively, as discussed in the text.

Figure 4. Electronic transport data on CoS_2-contacted FeS_2 crystals doped to room temperature Hall electron densities (n(300 K)) ≈ 1×10^{17} cm^{-3} with Co (a-d, red) and V_S (e-h, green). (The V_S-doped crystal is from Fig. 1(b)). Shown are the temperature (T) dependence ($\log_{10}$ scale) of: (a,e) the resistivity (ρ); (b,f) the low-magnetic-field Hall electron density (n); (c,g) the resulting Hall mobility (μ); and (d,h) the 9 T perpendicular-to-plane magnetoresistance, $MR(9T) = [\rho(B) - \rho(0)]/\rho(0)$. The Arrhenius fits to $n(T)$ in (b,f) yield the shown activation energies (ΔE). The power law fits to $\mu(T)$ in (c,g) yield the shown exponents. The insets in (a,e) are Zabrodskii plots (ln W *vs.* ln T, where $W = -d(\ln R)/d(\ln T)$), linearizing $\rho = \rho_0 \exp(T_0/T)^m$ and yielding the exponent m from the slope); the black lines correspond to $m = ½$, *i.e.*, Efros-Shklovskii variable-range hopping (ES VRH). The insets to (d,h) show the magnetic field (B) dependence of $ln[\rho(B)/\rho(0)]$ for Co- and V_S-doped crystals at 8 and 5 K, respectively; the black lines are fits to an ES VRH model yielding localization lengths (L_c) of 13 and 16 nm, respectively. Colored dashed lines connect the points, and vertical black dashed lines mark the diffusive-hopping crossovers.

Figure 5. Calculated band structure (left panels) and spin-polarized density-of-states (DOS, right panels) for (a) Co- and (b) V_S-doped pyrite. The green horizontal line marks the Fermi energy, the zero of energy is at the valence band maximum, and the DOS is shown for the two spin-states. As described in the main text and in Supplemental Material Sec. H [29], these calculations involve $3 \times 3 \times 3$ supercells containing one Co_{Fe} defect (in (a)) and a tetra-S-vacancy (in (b)). In all cases, a Hubbard $U = 1.8$ eV was used on Fe, as optimized in prior work [17]. For the Co in (a), as discussed in Supplemental Material, the $U = 3$ eV result is shown.

Figure 6. Ratio of the Hall electron densities (n_H/n_L) extracted at high ($|B| \geq 7$ T) and low ($|B| \leq 1$ T) magnetic fields in the (a) Co-doped and (b) V_S-doped FeS_2 crystals in Fig. 4. The insets show transverse (Hall) resistance (R_{xy}) *vs.* B at 40 and 12 K for the Co- and V_S-doped crystals, respectively (*i.e.,* the temperatures at which the non-linearity in $R_{xy}(B)$ is maximum).

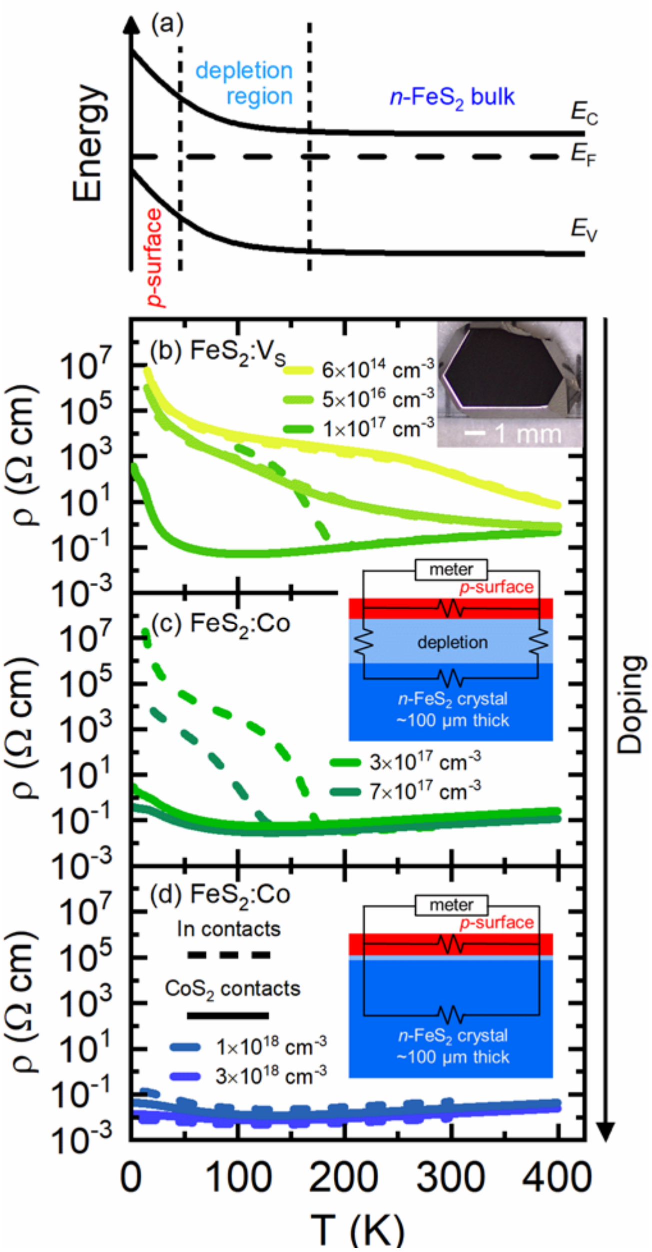
(a)
Energy
depletion region
n-FeS2 bulk
EC
EF
EV
p-surface
(b) FeS2:VS
6×10^14 cm^-3
5×10^16 cm^-3
1×10^17 cm^-3
1 mm
meter
p-surface
depletion
n-FeS2 crystal ~100 µm thick
(c) FeS2:Co
3×10^17 cm^-3
7×10^17 cm^-3
(d) FeS2:Co
In contacts
CoS2 contacts
1×10^18 cm^-3
3×10^18 cm^-3
ρ (Ω cm)
10^7
10^5
10^3
10^1
10^-1
10^-3
Doping
0
100
200
300
400
T (K)

Figure 1

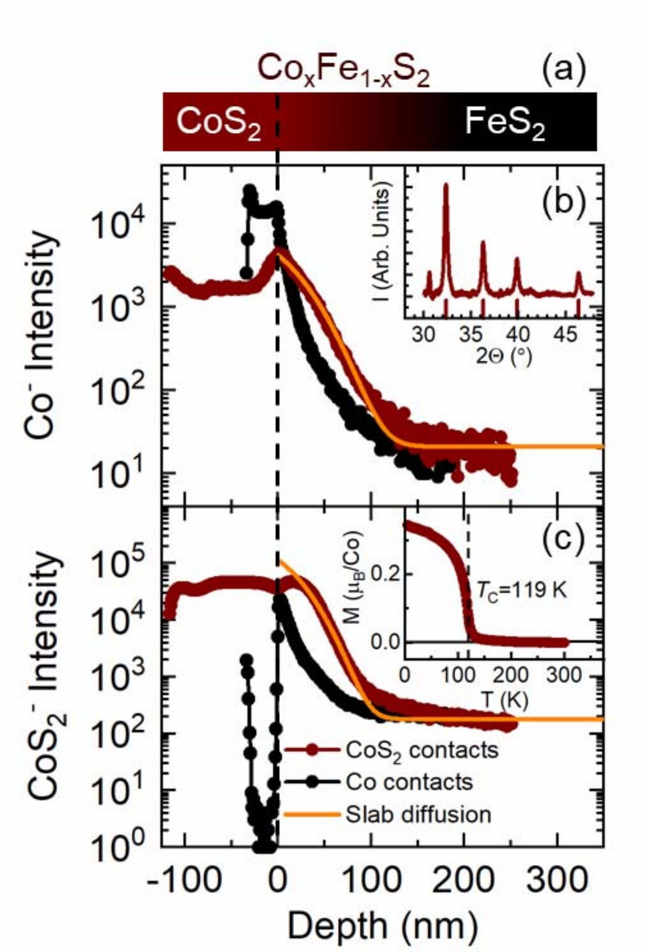
$Co_xFe_{1-x}S_2$
(a)
CoS_2
FeS_2
(b)
I (Arb. Units)
30
35
40
45
2Θ (°)
Co^- Intensity
10^4
10^3
10^2
10^1
(c)
M (μ_B/Co)
0.2
0.0
T_C=119 K
0
100
200
300
T (K)
CoS_2^- Intensity
10^5
10^4
10^3
10^2
10^1
10^0
CoS_2 contacts
Co contacts
Slab diffusion
-100
0
100
200
300
Depth (nm)

Figure 2

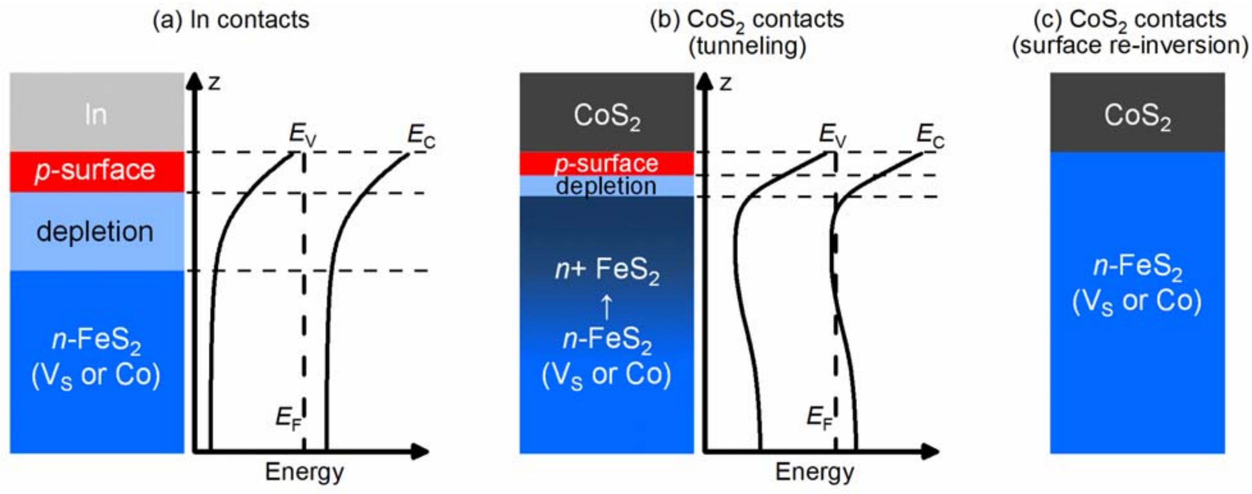
(a) In contacts
In
p-surface
depletion
n-FeS2
(VS or Co)
z
EV
EC
EF
Energy
(b) CoS2 contacts
(tunneling)
CoS2
p-surface
depletion
n+ FeS2
↑
n-FeS2
(VS or Co)
z
EV
EC
EF
Energy
(c) CoS2 contacts
(surface re-inversion)
CoS2
n-FeS2
(VS or Co)

Figure 3

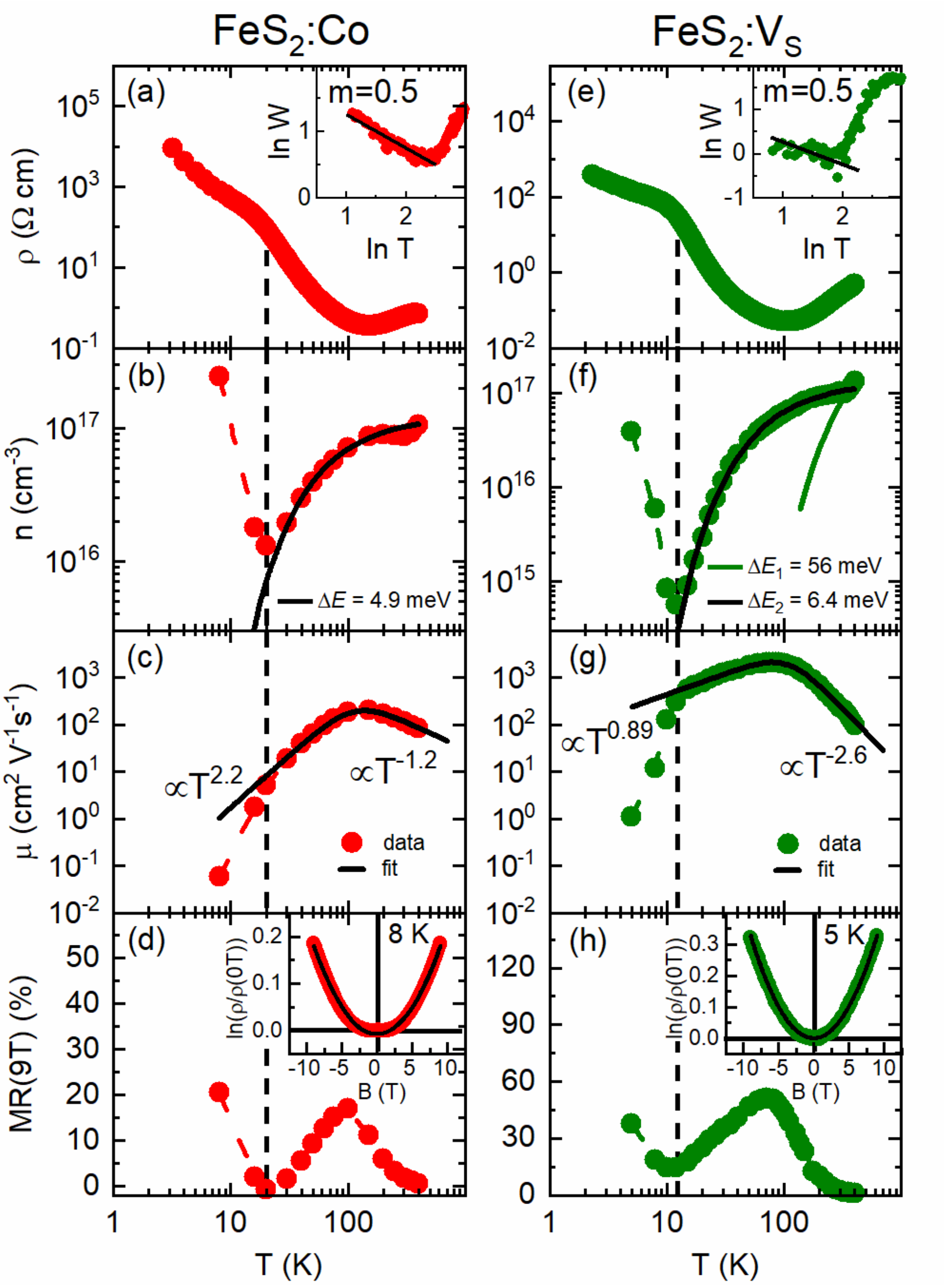
FeS2:Co
FeS2:VS
(a)
ρ (Ω cm)
10^5
10^3
10^1
10^-1
m=0.5
ln W
ln T
0
1
2
(b)
n (cm^-3)
10^17
10^16
ΔE = 4.9 meV
(c)
μ (cm^2 V^-1s^-1)
10^3
10^2
10^1
10^0
10^-1
10^-2
∝T^2.2
∝T^-1.2
data
fit
(d)
MR(9T) (%)
50
40
30
20
10
0
8 K
ln(ρ/ρ(0T))
0.2
0.1
0.0
-10
-5
0
5
10
B (T)
T (K)
1
10
100
(e)
10^4
10^2
10^0
10^-2
m=0.5
ln W
ln T
1
0
-1
2
(f)
10^17
10^16
10^15
ΔE1 = 56 meV
ΔE2 = 6.4 meV
(g)
∝T^0.89
∝T^-2.6
data
fit
(h)
120
90
60
30
0
5 K
ln(ρ/ρ(0T))
0.3
0.2
0.1
0.0
B (T)
T (K)

Figure 4

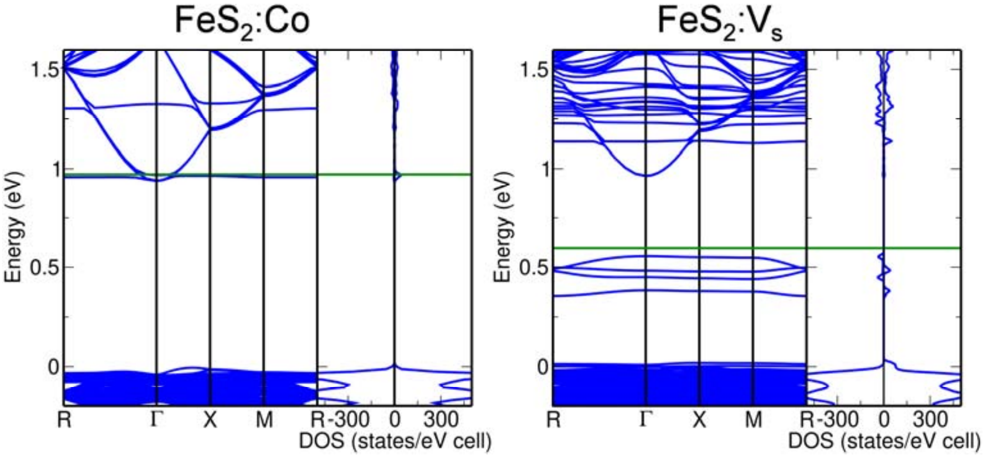

FeS_2:Co
FeS_2:V_s
Energy (eV)
1.5
1
0.5
0
R
Γ
X
M
R
-300
0
300
DOS (states/eV cell)

Figure 5

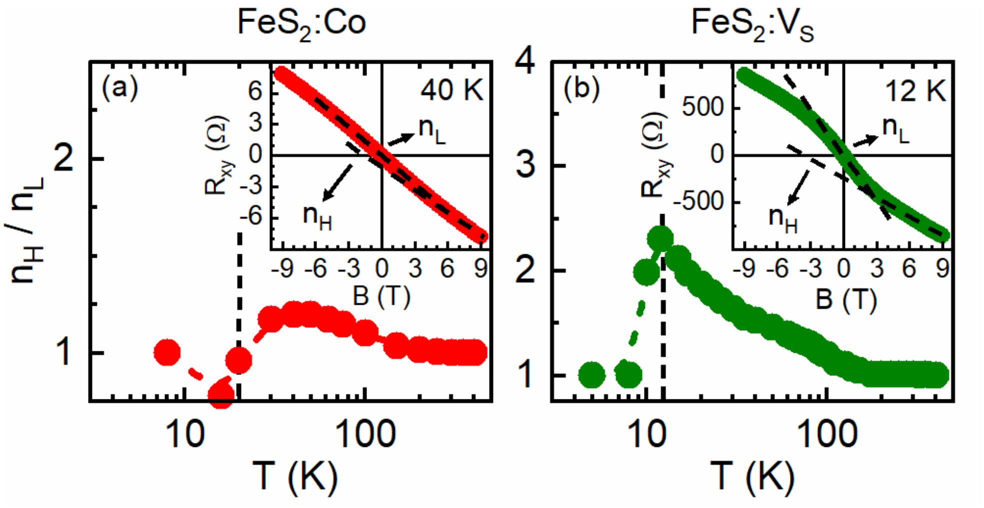
FeS$_2$:Co
FeS$_2$:V$_S$
(a)
(b)
n_H / n_L
1
2
3
4
10
100
T (K)
40 K
12 K
R_{xy} (Ω)
6
3
0
-3
-6
500
-500
B (T)
-9 -6 -3 0 3 6 9
n_L
n_H

Figure 6